Optics Letters

Anomalous and near-zero group-velocity dispersion in the sub-THz and mm-band atmospheric windows

A. A. Voronin[1,2,3] and A. M. Zheltikov[1,2,3,4,*]

[1]Physics Department, International Laser Center, M. V. Lomonosov Moscow State University, Moscow 119992, Russia
[2]Department of Physics and Astronomy, Texas A&M University, College Station, Texas 77843, USA
[3]Russian Quantum Center, 143025 Skolkovo, Moscow Region, Russia
[4]Moscow Institute of Physics and Technology, Dolgoprudny, Moscow Region 141701, Russia
*Corresponding author: zheltikov@physics.msu.ru

Received 5 March 2019; revised 7 April 2019; accepted 18 April 2019; posted 22 April 2019 (Doc. ID 361653); published 14 June 2019

Analysis of the complex refractive index of atmospheric air reveals remarkably broad and continuous regions of anomalous and near-zero group-velocity dispersion in the subterahertz (sub-THz) and millimeter-band atmospheric windows. One such broadband dispersion anomaly is shown to occur in the high-frequency wing of the 60-GHz band of molecular oxygen. Adjacent to this dispersion anomaly is a broadband atmospheric transparency region within which the group-velocity dispersion is unusually weak, enabling distortion-free long-distance transmission of broadband millimeter-wave field waveforms, as well as broadband remote sensing in the millimeter band. Although broad regions of anomalous and near-zero dispersion also exist in the sub-THz range, their utility for long-distance transmission and remote sensing is limited because of strong atmospheric absorption.

https://doi.org/10.1364/OL.44.003170

Optical physics is rapidly expanding its realm toward lower frequencies, beyond the borders of the visible, infrared (IR), and even terahertz (THz) spectral ranges [1–4]. As one of the major trends, concepts and methods of ultrafast photonics find growing use in microwave technologies, opening new horizons in long-distance transmission of microwave signals [5,6]. Integration of microwaves with ultrashort high-intensity laser pulses has been shown to offer much promise for the generation of long-lived laser filaments and remote sensing [7,8].

Bounded by microwave and THz regions lies the millimeter-wave (MMW) frequency band—the range of particular significance for radio astronomy, remote sensing, as well as telecommunication, medical, and security-screening applications [9–11]. Central to understanding the potential of ultrafast-optics methods extended to these applications is the search for broad regions of anomalous, zero, and near-zero group-velocity dispersion (GVD), where broadband electromagnetic field waveforms could be transmitted through atmospheric air with minimal or even no distortions. In the visible and near-IR ranges, such an analysis is greatly facilitated by a detailed knowledge of the refractive properties of atmospheric air. In these spectral regions, the refraction of Earth's atmosphere is routinely described in terms of a closed-form Sellmeier equation, whose phenomenologic coefficients have been defined with very high accuracy [12–15]. In the longer-wavelength range, however, within a broad spectral region spanning from the mid-IR all the way to the microwave range, the windows of high transparency of the atmosphere alternate with absorption bands related to molecular transitions, which give rise to rapidly oscillating frequency dependences of the complex refractive index. Such a behavior of air refraction greatly complicates the search for anomalous-, zero-, and near-zero-GVD regions beyond the visible and near-IR atmospheric windows. Still, as shown in a recent work [16], a compact, closed-form generalization of the Sellmeier-equation description of air refraction and its dispersion is possible for a broad spectral range from the near- to the long-wavelength IR.

Whether or not this approach can be extended to even lower frequencies and applied to the MMW band is still an open question. Here, we show that such an extension is indeed possible. We present a physical model that enables an accurate quantitative analysis of the complex refractive index of atmospheric air in the sub-THz and MMW ranges, thus helping advance the understanding of broadband electromagnetic propagation phenomena in sub-THz and MMW atmospheric windows. This analysis reveals remarkably broad and continuous regions of anomalous and near-zero GVD in MMW atmospheric windows, enabling distortion-free long-distance transmission of broadband MMW field waveforms, as well as remote sensing in the MMW band. We will also show that, although broad regions of anomalous and near-zero GVD also exist in the sub-THz range, their utility for long-distance transmission and remote sensing is limited because of strong atmospheric absorption.

Our model is based on a generic equation for the complex refractive index of a gas-phase mixture of atoms and molecules:

$$n(\omega) = \sum_{q,j} \frac{N_q c^2 S_{qj}(T)}{\omega_{qj}} \times \left(\frac{1}{\omega - \omega_{qj} - i\Gamma_{qj}(p,T)} - \frac{1}{\omega + \omega_{qj} - i\Gamma_{qj}(p,T)} \right), \quad (1)$$

where N_q is the density of molecular or atomic species of sort q, $S_{qj}(T)$, ω_{qj}, $\Gamma_{qj}(p, T)$ are the strength, central frequency, and linewidth, respectively, of the jth spectral line of a molecule or atom of sort q, T is the temperature, and p is the pressure.

The strengths of the spectral lines are defined in our model as [17]

$$S_{qj}(T) = \frac{\pi}{2}\frac{cA_{qj}g_{qj}}{\omega_{qj}^2}\left[\exp\left(-\frac{E_{qj}^{(1)}}{k_B T}\right) - \exp\left(-\frac{E_{qj}^{(2)}}{k_B T}\right)\right]\frac{1}{Q_q(T)}, \tag{2}$$

where $E_{qj}^{(1)}$ and $E_{qj}^{(2)}$ are the energies of the lower and upper states, respectively, of a molecular or atomic transition with frequency ω_{qj}, A_{qj} is the spontaneous-emission Einstein coefficient for this transition, g_{qj} is the statistical weight of the upper state of this transition, $Q_q(T)$ is the pertinent partition function, and k_B is the Boltzmann constant.

The linewidths $\Gamma_{qj}(p, T)$ are calculated using the Voigt-profile approximation, $\Gamma_{qj}(p, T) = 0.53\Gamma_{qj}^{(1)}(p, T) + (0.22[\Gamma_{qj}^{(1)}(p, T)]^2 + [\Gamma_{qj}^{(2)}(T)]^2)^{1/2}$. Here, $\Gamma_{qj}^{(1)}(p, T) = (T_{\text{ref}}/T)^{n_{qj}}[\gamma_{qj}^{\text{self}}(p_q/p_{\text{atm}}) + \gamma_{qj}^{\text{air}}(p - p_q)/p_{\text{atm}})]$ is the collisional broadening linewidth, $\Gamma_{qj}^{(2)}(T) = (\omega_{qj}/(2\pi c)^2)\times(2N_A k_B T)^{1/2}(M_q)^{-1/2}$ is the Doppler linewidth, T_{ref} is the reference temperature, n_{qj} is the effective exponent, $\gamma_{qj}^{\text{self}}$ is the linewidth due to collisions of molecules or atoms of sort q with molecular or atomic species of the same sort at $T = T_{\text{ref}}$ and $p = 1$ atm, γ_{qj}^{air} is the linewidth due to collisions of molecules or atoms of sort q with molecular or atomic species of another sort at $T = T_{\text{ref}}$ and $p = 1$ atm, $p_q = N_q k_B T$ is the partial pressure of molecules or atoms of sort q, such that $p = \sum_q (N_q k_B T)$, M_q is the molar mass of species of sort q, and N_A is the Avogadro constant.

The values of A_{qj}, ω_{qj}, $\gamma_{qj}^{\text{self}}$, and γ_{qj}^{air} at $T_{\text{ref}} = 296$ K and $p = 1$ atm, as well as the parameters I_q, g_{qj}, $E_{qj}^{(1)}$, $E_{qj}^{(2)}$, and $Q_q(T)$ are taken from the HITRAN database [17]. The water vapor concentration is defined as $N_{H_2O} = hp_S(k_B T)^{-1}$, where h is the humidity, and p_S is the pressure of saturated water vapor [18]. Calculations are performed with standard assumptions regarding the content of atmospheric air, viz., $N(O_3):N(N_2O):N(CO):N(CH_4):N(O_2):N(NO):N(SO_2):N(NO_2):N(NH_3):N(OH):N(N_2):N(Ne):N(Kr):N(Ar):N(H_2):N(He) = 10^{-7}:3\cdot10^{-7}:10^{-7}:1.6\cdot10^{-6}:0.20946:5\cdot10^{-10}:5\cdot10^{-10}:10^{-9}:4\cdot10^{-7}:3.9\cdot10^{-13}:0.781:1.8\cdot10^{-5}:10^{-6}:9.34\cdot10^{-3}:5\cdot10^{-7}:5.2\cdot10^{-6}$. The air temperature in all the calculations presented below is taken equal to $T = 25$°C, the air humidity is set at $h = 50\%$, and the CO_2 density is $N(CO_2) = 500$ ppm.

Transmission of an electromagnetic field waveform through the atmosphere is modeled by solving a linear version of the field-evolution equation. The input field waveform is assumed to have a Gaussian pulse envelope with a pulse width τ_0 and a central frequency ω_0.

In Fig. 1(a), we present the absorption coefficient $\alpha(\omega) = \omega \cdot \text{Im}[n(\omega)]/c$ of atmospheric air in the sub-THz and MMW ranges calculated as a function of the frequency $\nu = \omega/(2\pi)$ using the model of Eq. (1) with only the strongest molecular bands included. Transmission properties of atmospheric air in this frequency range, as can be seen in Fig. 1(a), are largely determined by absorption bands of water and molecular oxygen, which show up as prominent peaks in the spectral profile of $\alpha(\omega)$. As a general tendency, the most intense absorption peaks in the sub-THz range, all due to rotational transitions of water (from ≈350 to 990 GHz in Fig. 1), are much stronger than the main absorption peaks in the MMW band, related to the Q-branch rotational transitions of O_2 [Figs. 1(a) and 2(a)] and the lowest-frequency rotational band of H_2O [Fig. 1(a)]. The CO_2 molecule, which gives rise to prominent GVD anomalies in the mid-IR range [16,19], does not show up in the refractive properties of air in the sub-THz and MMW ranges, since purely rotational transitions are incompatible with its symmetry. As can be seen in Fig. 1(a), typical absorption lengths $l_a = 1/\alpha$ in the sub-THz atmospheric windows are much shorter than typical l_a values in the MMW transparency regions. Specifically, while the longest absorption length around the center of the ≈850-GHz window, is less than 100 m, the absorption length within the ≈90-GHz window exceeds 10 km [Fig. 1(a) and the maroon curve in Fig. 2(b)].

Figure 1(b) displays the GVD coefficient $k_2 = \partial^2 k/\partial\omega^2$, with $k = k(\omega) = (\omega/c)\text{Re}[n(\omega)]$, calculated as a function of ν for the sub-THz and MMW ranges. We are particularly interested here in anomalous GVD, i.e., negative-k_2 regions [shown by red segments of the $k_2(\nu)$ dependence in Fig. 1(b)], as well as the regions where the GVD is close to zero, allowing dispersion-induced distortions of temporal envelopes and phase profiles of broadband electromagnetic field waveforms to be minimized. While causality dictates an anomalous GVD in a high-frequency wing of every isolated absorption line, for atmospheric air, situations in which such dispersion anomalies extend deep into a transparency range and are broad enough to support ultrashort electromagnetic radiation pulses are very rare. Only a few such GVD anomalies have been identified so far. Among those, dispersion anomalies occurring in the 3.6–4.1-μm and 9.0–12.5-μm wavelength ranges [16,19,20] are notable as they fall within practically significant atmospheric windows in the mid- and long-wavelength-IR and are readily accessible with the existing laser sources of ultrashort high-peak-power pulses [21], enabling soliton transmission regimes in atmospheric air [22].

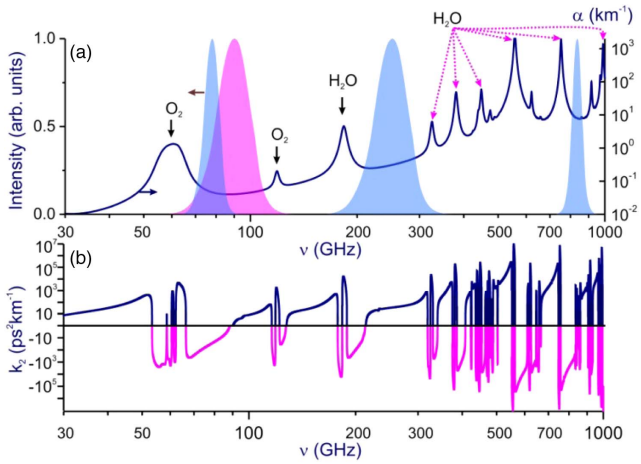

Fig. 1. Frequency dependences of (a) absorption coefficient α and (b) GVD coefficient k_2 of atmospheric air with $T = 25$°C, $h = 50\%$, and $N(CO_2) = 500$ ppm in the sub-THz and millimeter-wave ranges. Also shown are the spectra (blue and pink shading) of sub-THz and MMW field waveforms used in simulations.

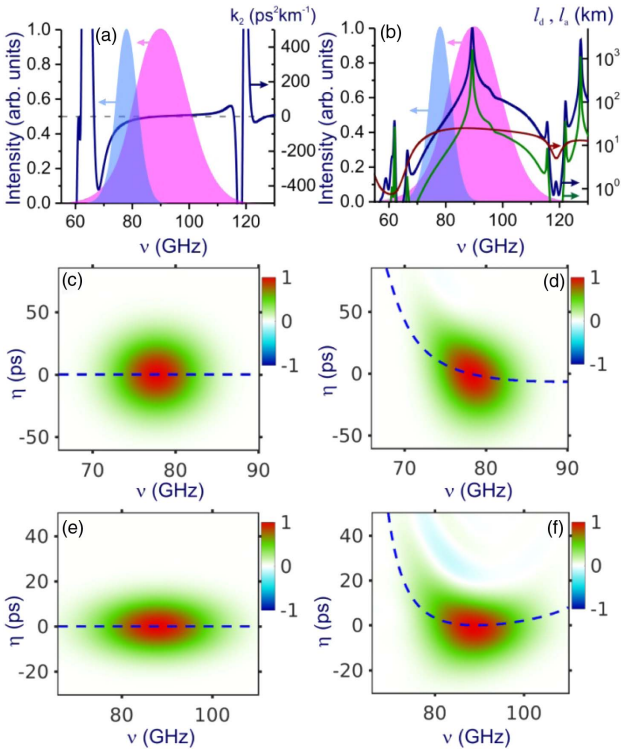

Fig. 2. (a), (b) Spectra of electromagnetic field waveforms with $\nu_0 = 78$ GHz and $\tau_0 = 50$ ps (blue shading) and $\nu_0 = 90$ GHz and $\tau_0 = 20$ ps (pink shading) against the spectral profiles of (a) GVD coefficient k_2, (b) absorption length (maroon curve), and dispersion length for a pulse with $\nu_0 = 78$ GHz and $\tau_0 = 50$ ps (blue curve) and $\nu_0 = 90$ GHz and $\tau_0 = 20$ ps pulse (green curve). (c)–(f) Wigner maps of the input (c), (e) and output (d), (f) pulses with $\nu_0 = 78$ GHz and $\tau_0 = 50$ ps (c), (d) and $\nu_0 = 90$ GHz and $\tau_0 = 20$ ps (e), (f). The relative group delay $\Delta\tau_g(\omega) = \tau_g(\omega) - \tau_g(\omega_0)$ is shown by the dashed line.

As an instructive example, calculations based on Eq. (1) reveal a broadband GDV anomaly in the sub-THz range occurring in the high-frequency wing of the strong H_2O absorption band centered at ≈750 GHz. This anomaly stretches from the edge of this H_2O absorption band all the way up to a zero-GVD point at $\nu_z \approx 830$ GHz. The utility of this dispersion anomaly is, however, limited because of low transmission of atmospheric air in the 850-GHz transparency window [Fig. 1(a)]. To illustrate this argument, we consider a pulse with $\nu_0 = 835$ GHz and $\tau_0 = 7$ ps, whose spectrum covers the weak-GVD region from ≈790 GHz to 880 GHz [Fig. 1(b)]. The maximum absorption length l_a in this frequency region is less than 100 m. Thus, even though the dispersion is low, with the dispersion length $l_d = \tau_0^2/|k_2|$ reaching ≈1 km at ≈840 GHz, long-distance transmission of broadband signals is not possible in this frequency range because of strong atmospheric absorption.

We now focus on the dispersion properties of atmospheric air within the high-transmission region lying between two absorption bands of molecular oxygen centered at ≈60 GHz and 120 GHz [Fig. 1(b)]. This frequency range is in many ways remarkable, as the high-frequency wing of the strong O_2 band at ≈60 GHz gives rise to a GVD anomaly that extends deep into the adjacent transparency window. Within a narrow spectral interval on the high-frequency wing of the ≈60-GHz O_2 absorption band, the GVD coefficient k_2 is very large in its magnitude and negative [Figs. 1(b) and 2(a)], as dictated by causality. Off this absorption band, k_2 rapidly decreases in its magnitude, reversing its sign at $\nu_z \approx 90$ GHz. A strong dispersion anomaly in the close vicinity of the O_2 absorption band, i.e., for $\nu < 62$ GHz, is of no or little practical value because of strong absorption. In the frequency range from ≈65 GHz to 90 GHz, however, the absorption length is sufficiently long, $l_a > 10$ km [maroon line in Fig. 2(b)], while the dispersion is still anomalous.

In Fig. 2, we illustrate typical broadband pulse evolution scenarios in this frequency range. With its central frequency set at $\nu_0 = 78$ GHz and its initial pulse width taken as $\tau_0 = 50$ ps, the field waveform shown by blue shading in Figs. 2(a) and 2(b) has its entire spectrum within the anomalous-GVD region [solid line in Fig. 2(a)]. Since $l_a >$ 10 km everywhere within the frequency range covered by the spectrum of this pulse [maroon curve in Fig. 2(b)], propagation paths $L \sim 10$ km are readily affordable. Specifically, within an $L = 8$ km path, the pulse is attenuated by 50% in its intensity and becomes stretched by air dispersion [cf. Figs. 2(c) and 2(d)]. Due to the anomalous GVD, the leading edge of the pulse is blue-shifted relative to the trailing edge.

For a map of dispersion-induced pulse-envelope, and phase distortions of a broadband field waveform, we resort to the Wigner function [23,24], $S(\omega,\eta) = \int_{-\infty}^{\infty} A(\eta+\zeta/2)A*(\eta-\zeta/2)\exp(-i\omega\zeta)\mathrm{d}\zeta$, where $A(\eta) = \int_0^{\infty} E(\omega)\exp(i\omega\eta)\mathrm{d}\omega$ is the complex electric field, and η is the retarded time. The Wigner function is uniquely suited for the purpose of our study here as, unlike cross-correlation frequency-resolved optical gating spectrograms, it provides a meaningful definition of the group delay $\tau_g(\omega)$ as a function of the instantaneous frequency $\omega = \omega(\eta)$—information that is central to dispersion analysis. Indeed, as one of its remarkable properties [23], the Wigner distribution $S(\omega,\eta)$ allows $\omega(\eta)$ and $\tau_g(\omega)$ to be consistently defined in terms of the expectation values $\langle\omega\rangle_\eta = [\int S(\omega,\eta)\mathrm{d}\omega]^{-1}\int \omega S(\omega,\eta)\mathrm{d}\omega$, and $\langle\eta\rangle_\omega = [\int S(\omega,\eta)\mathrm{d}\eta]^{-1}\int \eta S(\omega,\eta)\mathrm{d}\eta$ as $\langle\omega\rangle_\eta = \partial\varphi/\partial\eta = \omega(\eta)$ and $\langle\eta\rangle_\omega = \partial\psi/\partial\omega = \tau_g(\omega)$, where the φ and ψ are the temporal and spectral phases, respectively.

The Wigner map in Fig. 2(d) displays clear signatures of anomalous dispersion. Within a propagation path of $L = 8$ km, this pulse becomes blue-shifted in its leading edge and red-shifted on its back. For a better visualization of dispersion effects, the dashed lines in Figs. 2(c) and 2(d) show the relative group delay $\Delta\tau_g(\omega) = \tau_g(\omega) - \tau_g(\omega_0)$ of a frequency component ω with respect to the central frequency ω_0. In the Wigner diagram of the input pulse [Fig. 2(c)], $\Delta\tau_g(\omega)$ is represented by a horizontal line. However, when this pulse is transmitted over $L = 8$ km in atmospheric air, $\Delta\tau_g(\omega)$ becomes a monotonically decreasing function of the frequency everywhere within the Wigner map of the MMW field [Fig. 2(d)], indicating anomalous dispersion.

As another important observation, in a broad region adjacent to the ≈60–90-GHz GVD anomaly, the GVD of atmospheric air within its millimeter-band window is unusually weak, enabling distortion-free long-distance transmission of broadband low-frequency electromagnetic field waveforms. The weakness of atmospheric GVD in this frequency range is due to a balance between the anomalous dispersion provided by the

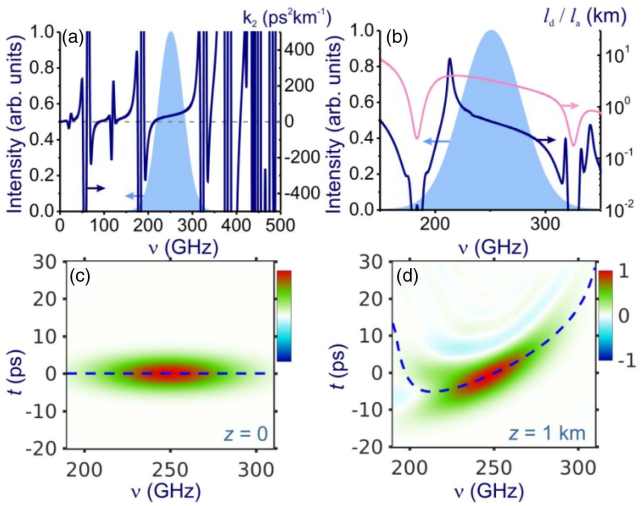

Fig. 3. (a) Spectrum of an electromagnetic field waveform with $\nu_0 = 250$ GHz and $\tau_0 = 7$ ps (shading) and the spectral profile of the GVD coefficient k_2 (solid line); (b) frequency dependences of the dispersion length (blue curve) and absorption length (pink curve); and (c), (d) Wigner maps of the input (c) and output (d) pulses. The relative group delay $\Delta\tau_g(\omega)$ is shown by the dashed line.

high-frequency tail of the 60-GHz band of oxygen and the normal GVD contributed by the ≈120-GHz band of O_2 [Figs. 1(a) and 1(b)], which partially, in a rough approximation, compensates anomalous GVD due to the 60-GHz band of O_2.

The Wigner maps in Figs. 2(e) and 2(f) illustrate the evolution of a MMW field waveform [pink shading in Figs. 2(a) and 2(b)] whose input pulse width, $\tau_0 = 20$ ps, corresponds to only 1.8 cycles of the field at the central frequency of this pulse, $\nu_0 = 90$ GHz. Behind an 8-km propagation path, the pulse appears almost undistorted [cf. Figs. 2(e) and 2(f)]. Small pulse-envelope and phase-profile distortions are barely visible only on the pulse edges [Fig. 2(f)] and are largely due to strong high-order dispersion effects, related to a steep GVD profile at the edge of the O_2 absorption band, i.e., for $\nu < 75$ GHz. Within the central part of the spectrum of the pulse, for ν ranging from ≈82 GHz to 97 GHz, the relative group delay $\Delta\tau_g(\omega)$ is represented by an almost horizontal line, indicating the remarkable weakness of the GVD.

A group-delay slope of an opposite sign would be a typical feature of a MMW field waveform when subject to a normal dispersion of atmosphere. This regime of field evolution is illustrated in Fig. 3. Here, a pulse with $\nu_0 = 250$ GHz and $\tau_0 = 7$ ps, whose entire spectrum falls within the range of normal dispersion of atmospheric air [Fig. 3(a)], acquires a noticeable chirp within $L = 1$ km [cf. Figs. 3(c) and 3(d)]. This chirp along with strong pulse stretching is readily seen in the Wigner map in Fig. 3(d). Now, the relative group delay $\Delta\tau_g(\omega)$ is a monotonically growing function of the frequency everywhere within the Wigner map [Fig. 3(d)], as the sign of the group delay in this frequency range is opposite to the sign of τ_g in the anomalous-GVD region [Fig. 2(d)].

To summarize, we have shown that atmospheric dispersion features remarkably broad and continuous regions of anomalous and near-zero GVD in the sub-THz and MMW windows. One such broadband dispersion anomaly exists in the high-frequency wing of the 60-GHz band of molecular oxygen, stretching from the edge of the O_2 absorption band all the way up to the zero-GVD frequency at ≈90 GHz, thus extending deep inside the high-transmission region of atmospheric air, where the absorption length exceeds 10 km. Adjacent to this dispersion anomaly is a broadband atmospheric transparency region within which the GVD of atmospheric air is unusually weak, enabling distortion-free long-distance transmission of broadband MMW field waveforms, as well as remote sensing in the MMW band. Although broad regions of anomalous and near-zero GVD also exist in the sub-THz range, their utility for long-distance transmission and remote sensing is limited because of strong atmospheric absorption.

Funding. Russian Foundation for Basic Research (RFBR) (18-29-20031, 16-32-60164, 18-02-40034); Russian Science Foundation (RSF) (17-12-01533—broadband spectrochronography); Welch Foundation (A-1801-20180324); Office of Naval Research Global (ONRG) (00014-16-1-2578).

REFERENCES

1. J. Capmany and D. Novak, Nat. Photonics **1**, 319 (2007).
2. Z. Jiang, C. B. Huang, D. E. Leaird, and A. M. Weiner, Nat. Photonics **1**, 463 (2007).
3. D. Marpaung, J. Yao, and J. Capmany, Nat. Photonics **13**, 80 (2019).
4. Z. Kudyshev, M. C. Richardson, and N. M. Litchinitser, Nat. Commun. **4**, 2557 (2013).
5. R. R. Musin, M. N. Shneider, A. M. Zheltikov, and R. B. Miles, Appl. Opt. **46**, 5593 (2007).
6. M. Châteauneuf, S. Payeur, J. Dubois, and J.-C. Kieffer, Appl. Phys. Lett. **92**, 091104 (2008).
7. A. M. Zheltikov, M. N. Shneider, and R. B. Miles, Appl. Phys. B **83**, 149 (2006).
8. M. N. Shneider, A. M. Zheltikov, and R. B. Miles, J. Appl. Phys. **108**, 033113 (2010).
9. T. S. Rappaport, R. W. Heath, R. C. Daniels, Jr., and J. N. Murdock, *Millimeter Wave Wireless Communications* (Prentice Hall, 2014).
10. S. Koenig, D. Lopez-Diaz, J. Antes, F. Boes, R. Henneberger, A. Leuther, A. Tessmann, R. Schmogrow, D. Hillerkuss, R. Palmer, T. Zwick, C. Koos, W. Freude, O. Ambacher, J. Leuthold, and I. Kallfass, Nat. Photonics **7**, 977 (2013).
11. A. Motes, *Free-Space Laser Communications: An Introduction* (AM Photonics, 2016).
12. H. Barrell and J. E. Sears, Philos. Trans. R. Soc. London A **238**, 1 (1939).
13. B. Edlén, J. Opt. Soc. Am. **43**, 339 (1953).
14. E. R. Peck and K. Reeder, J. Opt. Soc. Am. **62**, 958 (1972).
15. P. E. Ciddor, Appl. Opt. **35**, 1566 (1996).
16. A. A. Voronin and A. M. Zheltikov, Sci. Rep. **7**, 46111 (2017).
17. L. S. Rothman, I. E. Gordon, Y. Babikov, A. Barbe, D. Chris Benner, P. F. Bernath, M. Birk, L. Bizzocchi, V. Boudon, L. R. Brown, A. Campargue, K. Chance, E. A. Cohen, L. H. Coudert, V. M. Devi, B. J. Drouin, A. Fayt, J. M. Flaud, R. R. Gamache, J. J. Harrison, J. M. Hartmann, C. Hill, J. T. Hodges, D. Jacquemart, A. Jolly, J. Lamouroux, R. J. LeRoy, G. Li, D. A. Long, O. M. Lyulin, C. J. Mackie, S. T. Massie, S. Mikhailenko, H. S. P. Müller, O. V. Naumenko, A. V. Nikitin, J. Orphal, V. Perevalov, A. Perrin, E. R. Polovtseva, C. Richard, M. A. H. Smith, E. Starikova, K. Sung, S. Tashkun, J. Tennyson, G. C. Toon, V. G. Tyuterev, and G. Wagner, J. Quant. Spectrosc. Radiat. Transfer **130**, 4 (2013).
18. A. Saul and W. Wagner, J. Phys. Chem. Ref. Data **16**, 893 (1987).
19. A. A. Voronin and A. M. Zheltikov, Opt. Lett. **42**, 3614 (2017).
20. A. A. Voronin and A. M. Zheltikov, Phys. Rev. A **95**, 023826 (2017).
21. A. V. Mitrofanov, A. A. Voronin, D. A. Sidorov-Biryukov, M. V. Rozhko, E. A. Stepanov, A. B. Fedotov, V. Shumakova, S. Ališauskas, A. Pugžlys, A. Baltuška, and A. M. Zheltikov, Sci. Rep. **7**, 2103 (2017).
22. A. V. Mitrofanov, A. A. Voronin, M. V. Rozhko, D. A. Sidorov-Biryukov, A. B. Fedotov, A. Pugžlys, V. Shumakova, S. Ališauskas, A. Baltuška, and A. M. Zheltikov, Optica **4**, 1405 (2017).
23. L. Cohen, *Time–Frequency Analysis* (Prentice Hall, 1995).
24. I. A. Walmsley and C. Dorrer, Adv. Opt. Photon. **1**, 308 (2009).